The Impact of the Different Geometrical Restrictions on the Nonadiabatic Photoisomerization of Biliverdin Chromophore

Yuan Fang[1,2], Haiyi Huang[1,2], Kunni Lin[1,2], Chao Xu[2,3*], Feng Long Gu[2,3*], Zhenggang Lan[2,3*]

[1]School of Chemistry, South China Normal University, Guangzhou 510006, China.

[2]MOE Key Laboratory of Environmental Theoretical Chemistry, South China Normal University, Guangzhou 510006, P. R. China.

[3]SCNU Environmental Research Institute, Guangdong Provincial Key Laboratory of Chemical Pollution and Environmental Safety, School of Environment, South China Normal University, Guangzhou 510006, P. R. China.

Email: 2020022489@m.scnu.edu.cn, zhenggang.lan@m.scnu.edu.cn

Abstract: The photoisomerization mechanism of the chromophore of bacterial biliverdin (BV) phytochromes is explored with the nonadiabatic dynamics simulation by using the on-the-fly trajectory surface-hopping method at the semi-empirical OM2/MRCI level. Particularly, the current study focuses on the influence of the geometrical constrains on the nonadiabatic photoisomerization dynamics of the BV chromophore. Here a rather simplified approach is employed in the nonadiabatic dynamics to capture the features of geometrical constrains, which adds the mechanical restriction on the specific moieties of the BV chromophore. This simplified method provides a rather quick approach to examine the influence of the geometrical restrictions on the photoisomerization. As expected, different constrains bring the distinctive influences on the photoisomerization mechanism of the BV chromophore, giving either strong or minor modification of both involved reaction channels and excited-state lifetimes after the constrains are added in different ring moieties. These observations not only contribute to the primary understanding of the role of the spatial restriction caused by biological environments in photoinduced dynamics of the BV chromophore, but also provide useful ideas for the artificial regulation of the photoisomerization reaction channels of phytochrome proteins.

1. Introduction

Phytochromes are photosensitive proteins, which are widely found in plants, bacteria and algae.[1] Plant phytochrome (PΦB) promotes the seed germination and the chlorophyll synthesis in plants.[2] Phycocyanin (PCB) and biliverdin (BV) phytochromes that are found in algae and bacteria, respectively, can synthesize biological pigments and promote growth.[3–5] In addition, BV was also used to design the near-infrared fluorescent proteins in the research of diseases such as cancers.[6–10] Owing to their importance, phytochromes have been extensively studied over decades.[9,11–18]

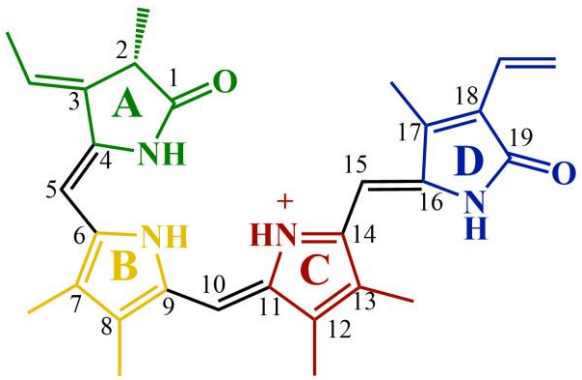

Figure 1. BV model in Pr (*ZsZsZa*) configuration

The biological functions of phytochrome are controlled by the switching between two forms (Pr and Pfr).[19] The physiologically inactive Pr form can absorb red light, and converts to the active Pfr form. In the reversed process, the Pfr form can return to the Pr form by absorbing far-red light. The switching between them drives the structural rearrangement in the phytochrome proteins to realize important biological functions.

The central chromophore of phytochrome is a methylene-bridged linear tetrapyrrole compound with several twisted carbon-carbon single and double bonds, resulting in the

existence of many isomers. In order to label these configurations, the bridged carbon-carbon double and single bonds are defined as *Z/E* and *syn/anti(s/a)* isomerism, respectively. Some studies have determined that the Pr of PΦB is in the *ZaZsZa* form,[20] while the Pr of PCB and BV has the *ZsZsZa* form (Figure 1).[21,22] In contrast, the Pfr configuration is still not fully clarified, which may be dependent on Pr → Pfr photoreaction processes.[23] Therefore, the study of Pr → Pfr reaction not only deepens the understanding of the photoisomerization process, but also helps to determine the Pfr conformation.

Considerable efforts were made to understand the Pr → Pfr photoisomerization mechanism. The photoisomerization process of BV and PΦB in the protein environments is believed to be around the $C_{15}C_{16}$ double bond.[24–29] Differently, Ulijasz et al. proposed that the twist of C_4C_5 double bond is the key to the isomerization of PCB.[23] At the same time, some studies also pointed out that the rotation of the $C_{10}C_{11}$ double bond was noticeable in the BV and PΦB isomerization,[30–32] at least in the gas phase. In addition, the hydrogen-bond network patterns greatly affect the photoisomerization channels of central chromophores, when different deprotonation status exist in these pyrrole rings.[33,34] These works demonstrated that the photoisomerization of phytochrome chromophores may be adjusted by the distinctive confinement of chromophores in the vacuum and in the surrounding environment. In a vacuum, the chromophore is a "free" molecule and the rotation of any carbon-carbon bond is not affected by external factors. In living organisms, nonetheless, chromophores can be spatially constrained by their surrounding residuals, placing additional

restrictions on their photoisomerization process. For example, one common idea is that Ring D in BV (Figure 1) and PΦB is not rigorously constrained due to the fact that it is located in a relatively loose protein cavity.[25,35] This leads to a high chance to realize the rotation of Ring D. This view was also supported by the work of Burgie et al., who showed that Ring A and Ring B are sandwiched in protein secondary domains and covalently linked to the protein for PΦB.[25] In addition, the C_{10} methyl bridge between Ring B and Ring C is tightly wrapped by surrounding residues in BV, preventing the photoisomerization at the C_{10} position.[21]

Here, we are interested in several detailed aspects of the photoisomerization mechanism of the BV chromophore. The BV chromophore attracts our attention due to its unique properties.[16,20,36] It is not only the chromophore of phytochrome in Deinococcus radiodurans, but also the heme-metabolism intermediate of all aerobic organisms.[7,8,37] It can be engineered into monomeric infrared fluorescent proteins (IFPs)[38,39] that may be potentially used in disease diagnosis.[6,9]

In the present work, we specifically focus on the possible influences of the restricted motions in the BV chromophore. Particularly, we wish to provide a rather preliminary view of the steric effects by surrounding environments on the photoisomerization though a quick computational study, instead of giving a very comprehensive description of the role of realistic environments in nonadiabatic dynamics. Therefore, the efficient treatment of the spatial constraints becomes very essential. In principle, the dynamics of molecules constrained by the biological environment can be simulated by the quantum mechanical/molecular mechanics (QM/MM) method, which can include all

degrees of freedom of the protein environment and solution compounds explicitly.[40–44] However, it requires rather large computational costs once performing the nonadiabatic dynamics simulations. Instead, we wish to treat the geometrical restriction in the nonadiabatic dynamics using a rather simplified approach with much less computational cost. Previously, many efforts have been made to mimic the biological environmental influence on the nonadiabatic dynamics in the simplified way. For example, Warshel simulated the restriction of protein by constraining the movements of terminal atoms in retinal molecules, rather than considering the motions of all atoms.[45] Barbatti et al. imposed the geometrical constraints by increasing the nuclear mass of the terminal hydrogen atom in the nonadiabatic dynamics simulation of the protonated Schiff bases linked to proteins.[46] This idea was also successfully used to study the environmental effects in the photochemistry of aminopyrimidines.[47–49] The employment of this "heavy-mass" approach shows many advantages: it can greatly reduce the computational costs and is easy to implement in the nonadiabatic dynamics simulations. Inspired by these works, we decide to take a similar idea in the trajectory surface hopping (TSH) simulations. The geometrical restriction of the surrounding environments is taken into account by using the very heavy atomic mass in the restricted moieties of the BV chromophore. We hope to elucidate the role of the possible surrounding environment on the photoinduced nonadiabatic processes, and further deepen the understanding of the photoisomerization mechanism of the BV chromophore in biological proteins.

2. Computational Details

2.1 Electronic Structure Calculation

The electronic structure calculations were performed with the semi-empirical orthogonalized-model (OM2) method.[50] The excited-state wave function was described by the multireference configuration interaction (MRCI) method within the configuration interaction scheme based on the Graphical Unitary Group Approach (GUGA-CI).[51,52] The molecular orbitals were generated by using the restricted open-shell Hartree-Fock (ROHF) approach. All electronic configurations were generated from five reference configurations [the closed-shell, two single (HOMO-1 to LUMO and HOMO to LUMO) and two double (HOMO-1 to LUMO and HOMO to LUMO) excitations]. The active space (16, 12) was employed which distributes 16 electrons in 12 orbitals: six π orbitals, two n orbitals and four π^* orbitals. The state minima (S_0_min and S_1_min) and minimum-energy S_0/S_1 conical intersection (CI) geometries were optimized.[53] To get a direct view of the excited-state reaction pathways, we constructed the potential energy (PE) profiles by linear interpolation of the internal coordinates (LIICs) from the ground-state minimum to the minimum-energy CI structures. All semi-empirical calculations were performed by using the MNDO2020 package.[54]

2.2 Nonadiabatic Dynamics

The photoinduced nonadiabatic dynamics were simulated by the on-the-fly TSH simulations at the OM2/MRCI level. Previous works have demonstrated that this approach provides an efficient and reasonable description on the excited-state

nonadiabatic dynamics or polyatomic systems with low computational cost.[32,55] A set of initial conditions (geometry and velocity) were generated using Winger sampling method.[56] All trajectories start from the first excited state. The time steps for the propagation of the nuclear and electron motions were 0.5 fs and 0.005 fs, respectively. The trajectories propagated up to 2000 fs. The nuclear motion was integrated by the velocity-Verlet method. The solution of the electron motion was carried out by the unitary propagation. The hopping probability was calculated with Tully's fewest switches algorithm.[57] All relevant energies, gradients and nonadiabatic couplings were calculated in the manner of on-the-fly along the trajectory propagation. A practical way proposed by Granucci et al. with the γ = 0.1 Hartree was employed to take the decoherence correction into account.[58] When hops take place, the velocity rescaling is performed according to the nonadiabatic coupling vector. For frustrated hops, the velocity component along the nonadiabatic coupling vector was reversed. The interface between the TSH dynamics module in the JADE package[59] and the electronic-structure calculations OM2/MRCI in the MNDO package was employed for the nonadiabatic dynamics simulations.

2.3 Molecular model construction

All calculations were simulated using a simplified model with the *ZsZsZa* structure that was identified as the main isomer of the Pr form in BV photochrome.[21] Here, several side groups (thioether bonds, propionic acid carboxyl groups on Rings B and C) should have minor contribution on the skeleton motion in the excited state dynamics,

we simply replaced them by the methyl group to reduce computational costs.

We wish to gain a deep understanding of the steric effect on the photoisomerization dynamics of BV molecules. Here, the BV molecules possess four five-membered rings. To get a full understanding of the impacts of different geometrical constraints, we considered as many restriction situations as possible, and totally constructed nine models, as shown in Table 1 and Figure 1. **Model 0** represents the original simplified BV chromophore model. In **Models I-IV**, a single ring is constrained. In **Models V-VII**, two adjacent rings were constrained, along with their connecting parts. We also built **Model VIII**, in which two side rings (A and D in Figure 1) were constrained. On this basis, we set the atomic masses in the restricted part of the BV molecule to 99999999 au and the initial velocity to 0 in the nonadiabatic dynamics simulation.

According to the simulation results (see discussions below), nine models were divided into four groups with rather different decay features: Group 1 includes **Models 0, I, IV** and **VIII**; Group 2 includes **Models II** and **V**; Group 3 includes **Models III** and **VII**; and Group 4 includes **Model VI**.

Table 1. All BV models with different geometrical constraints. The constrained parts are labelled by different colors in Figure 1.

Models	Constrained part of the BV molecule	Group
0	-	1
I	Ring A (green part)	1
II	Ring B (yellow part)	2

III	Ring C (red part)	3
IV	Ring D (blue part)	1
V	Rings A and B (green part, C_5 methyl bridge and yellow part)	2
VI	Rings B and C (yellow part, C_{10} methyl bridge and red part)	4
VII	Rings C and D (red part, C_{15} methyl bridge and blue part)	3
VIII	Rings A and D (green part, and blue part)	1

3. Results and Discussion

3.1 CI Structures and Channels

The Pr→Pfr photoisomerization mechanism is closely related to the ultrafast nonadiabatic process governed by the conical intersections. To clarify the role of the CIs in the nonadiabatic dynamics, we optimized the several CI geometries (Figure 2). Table S1 and S2 (in supporting information (SI)) show the key internal coordinates at S_0_min, S_1_min and CIs. These four important CIs display the below geometrical features:

- CI_1: $C_9C_{10}C_{11}N_C$ dihedral angle rotates to -85.4° with the elongated $C_{10}C_{11}$ bond and the shortened C_9C_{10} bond;
- CI_2: $N_BC_9C_{10}C_{11}$ dihedral angle rotates to -93.4° with the elongated C_9C_{10} bond and the shortened $C_{10}C_{11}$ bond;
- CI_3: $C_{14}C_{15}C_{16}N_D$ dihedral angle rotates to 95.0° with the elongated $C_{15}C_{16}$ bond and the shortened $C_{14}C_{15}$ bond;
- CI_4: $N_AC_4C_5C_6$ dihedral angle rotates to 89.6° with the elongated C_4C_5 bond and the

shortened C_5C_6 bond.

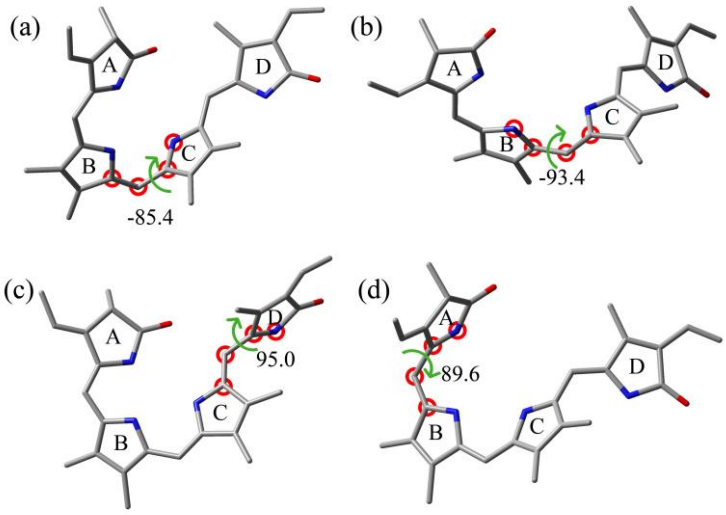

Figure 2. Four important S_0/S_1 minimum-energy CI structures and their major dihedral angles (marked by red circles) (a) CI_1; (b) CI_2; (c) CI_3; (d) CI_4.

To get a direct view of the excited-state reaction pathways, we constructed the PE profiles from the ground-state minimum to the CI structures. In Figure 3a and 3b, the excited-state pathways from S_0_min to both CI_1 and CI_2 are barrierless, and the former one is steeper. Moreover, the energy of CI_1 is lower than that of CI_2. While the other two channels towards CI_3 and CI_4 show some visible barriers (see Figure 3c and 3d), and the CI_4 channel exists a slightly higher energy barrier.

It is necessary to point out that the torsional motions at the $C_{14}C_{15}$ and C_5C_6 bonds also lead to the CIs, giving CI_5 and CI_6 (see Figure S1), respectively. However, as shown in Figure S2, the reaction pathways towards them display very high barriers, preventing the possibility of these two photoisomerization channels. Thus, we do not discuss them here.

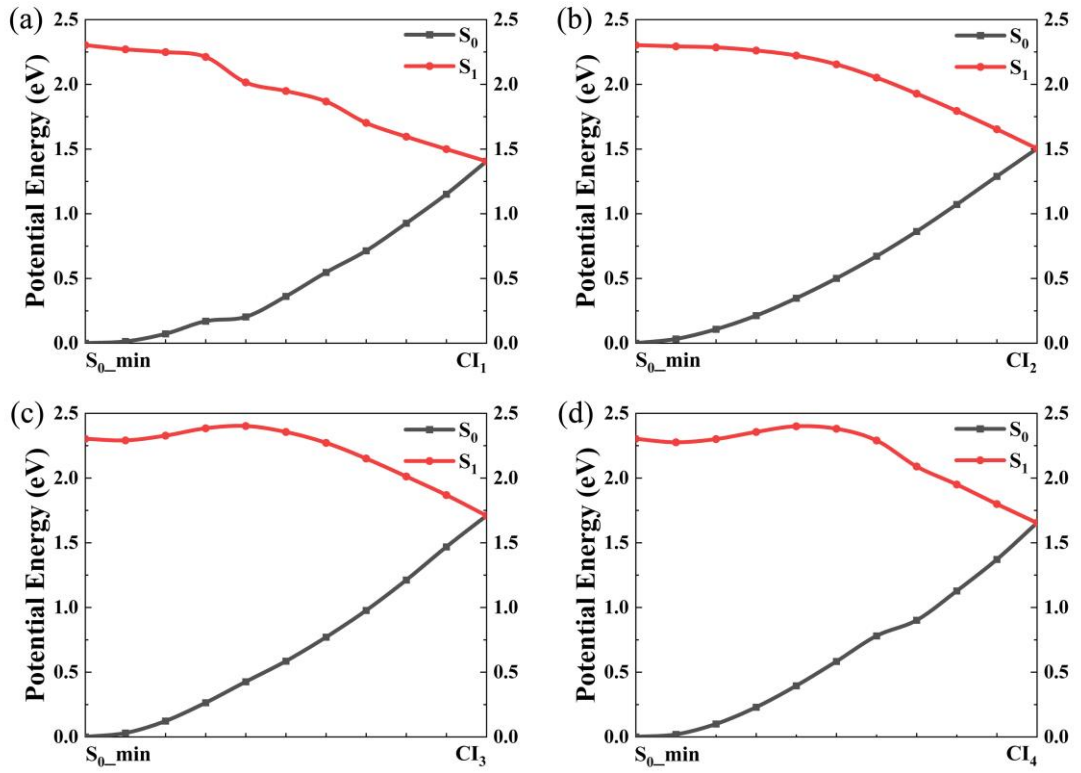

Figure 3. Potential energy curves along the linear interpolated pathway from S_0_min to the four conical intersections (a) CI_1; (b) CI_2; (c) CI_3; (d) CI_4.

3.2 Photoisomerization Pathways

We performed the nonadiabatic dynamics simulation for all nine models mentioned above. After collecting all hop geometries and analyzing their correlations with optimized CIs, four CIs (CI_1, CI_2, CI_3, and CI_4) were identified to play key roles in the nonadiabatic decay. By analyzing the hopping structures in TSH dynamics, we can divide all nine BV models into four groups according to their involved decay channels, as shown in Table 2.

Table 2. The branching ratio of different reaction channels in each constrained BV model, obtained from the TSH dynamics up to 2 ps.

Group	Model	CI_1	CI_2	CI_3	CI_4	No Hop
1	**0**	94.1%	5.9%	0.0%	0.0%	0.0%
	I (Ring A)	94.3%	1.0%	3.6%	0.0%	1.1%
	IV (Ring D)	95.7%	3.8%	0.0%	0.0%	0.5%
	VIII (Rings A and D)	87.0%	3.5%	0.0%	0.0%	9.5%
2	**II** (Ring B)	67.0%	1.1%	21.9%	0.0%	10.0%
	V (Rings A and B)	63.1%	1.4%	30.3%	0.0%	5.2%
3	**III** (Ring C)	45.5%	14.1%	4.3%	1.0%	35.1%
	VII (Rings C and D)	31.4%	13.3%	0.0%	6.4%	48.9%
4	**VI** (Rings B and C)	0.0%	0.0%	42.0%	8.0%	50.0%

The first group includes **Models 0**, **I**, **IV** and **VIII**. Among them, **Model 0** represents the free BV model. **Models I**, **II** and **VIII** refer to the situations in which the constraints are added in two terminal rings, namely Rings A, D and both, respectively. As shown in Table 2, Figure 4a and Figure S4, the CI_1 controlled pathway is the predominant decay channel in these four models. Following this channel, the trajectories experience the significant changing of the $C_9C_{10}C_{11}N_C$ angle up to ~85.4°, as shown in Figure 2. However, the other CIs only make very small contributions. For instance, the CI_2 plays a little role here, and the CI_3 channel only appears in the TSH dynamics of **Model I**. This result can be well understood by the PE curves. As we discussed previously, there is no barrier existing in the first excited-state decay pathways from S_0_min to CI_1 and CI_2, and the former PE surface is steeper. At the same time, the other two channels towards CI_3 and CI_4 display visible energy barriers along the excited-state pathways. As a consequence, in **Model 0**, the channel via CI_1 becomes dominant while only a

small number of trajectories decay via CI_2 here. Since the motions of Rings A and D are constrained in **Models I**, **IV** and **VIII**, we expect that the major torsional around the carbon-carbon double bond between Rings B and C should not be largely hindered. This explains why their nonadiabatic decay channels are similar to that of **Model 0**. Overall, the CI_1 pathway is the dominant channel in the nonadiabatic dynamics of **Models 0, I, IV** and **VIII** in Group 1, in which the photoisomerization mainly takes place at the $C_{10}C_{11}$ bond.

The second group includes **Model II** and **Model V**, with Ring B and Rings A and B are constrained, respectively. For these two models, most of trajectories decay via CI_1 while the secondary channel goes to the CI_3 (see Table 2, Figure 4b and Figure S5). Compared to the models in Group 1, the contributions of both CI_1 and CI_2 become decreased, while the role of CI_3 starts to be visible. The change of the branching ratio to different channels can be explained as follows. Once Ring A and Ring B are immobilized, the torsional motion along the C_9C_{10} bond becomes limited, resulting in the reducing of the CI_2 channel. In addition, the analysis of trajectory propagation clarifies that the motion of Ring B is necessary in the $C_{10}C_{11}$ isomerization channel, as shown in Figure S3 in SI for details. Therefore, the constrains on Ring B leads to the decreasing of the CI_1 channel. Due to the reducing of both CI_1 and CI_2 channels, trajectories should move by following either CI_3 or CI_4 channel, and both show barriers on the excited-state reaction pathway. Although the PE barrier in the CI_3 controlled channel is only 0.06 eV lower than that of the CI_4 dominated channel, the difference in the proportion of the channel is obvious. This feature may be attributed to the reasons

below. The nonadiabatic processes of the channels via CI_3 and CI_4 show distinctions in ring motions. The decay channel via CI_3 is mainly characterized by the motion of the Ring D. In the CI_4 channel, Ring A must experience the outward motion away from the other three rings first, and then rotate. Therefore, the CI_3 channel is easily achieved due to much less geometrical rearrangement. As a short summary, the CI_1 channel with the photoisomerization site at the $C_{10}C_{11}$ bond is still dominant in the nonadiabatic dynamics of Group 2. However, the branching ratio of this channel is reduced, with the increasing of the CI_3 channel that displays the photoisomerization at the $C_{15}C_{16}$ bond.

The third group includes **Models III** and **VII**, with Ring C constrained and Rings C and D constrained. As shown in Table 2, Figure 4c and Figure S6, the channel via CI_1 is still the most important one. Interestingly, we also see the secondary channels via CI_2. The dominant role of CI_1 and the secondary role of CI_2 are addressed in the previous discussions. Compared to **Model 0**, the proportion of CI_2 (CI_1) channel has increased (decreased) greatly. The analysis of trajectory evolution indicates that the torsion around the $C_{10}C_{11}$ bond is strongly controlled by the Ring C (see Figure S3). As a consequence, the restriction of Ring C leads to the decreasing of the CI_1 channel. The reducing of the CI_1 channel certainly improves the contributions of other channels. As the results, more trajectories follow the CI_2 because it is also barrierless. In addition, a few of trajectories choose the CI_3 channel with the smaller potential barrier. Since **Model VII** confines Rings C and D, the CI_3 channel of the $C_{15}C_{16}$ rotation between Rings C and D is closed. Therefore, there is no CI_3 channel in **Model VIII**, resulting in an increase in the proportion of CI_4 channels. Overall, the CI_1 channel with the

photoisomerization at the $C_{10}C_{11}$ bond is still dominant in Group 3, while its ratio is largely reduced. The secondary channel is governed by the CI_2 that shows the isomerization site at C_9C_{10} bond.

The fourth group includes only **Model VI**, in which both two central Rings, B and C are constrained. In this model, the vast majority of the trajectories decay through CI_3 and small number of trajectories decay via CI_4, see Table 2, Figure 4d and Figure S7. Since both Rings B and C are restricted, the dihedral angle between them almost cannot rotate, leading to the vanishing of the CI_1 and CI_2 channels. Due to the less geometrical rearrangement discussed above, the CI_3 channel is dominant one in Group 4. In this case, the photoisomerization mainly takes place at the $C_{15}C_{16}$ site. Nevertheless, this model shows the similar geometrical constraints at the BV chromophore in protein environments.

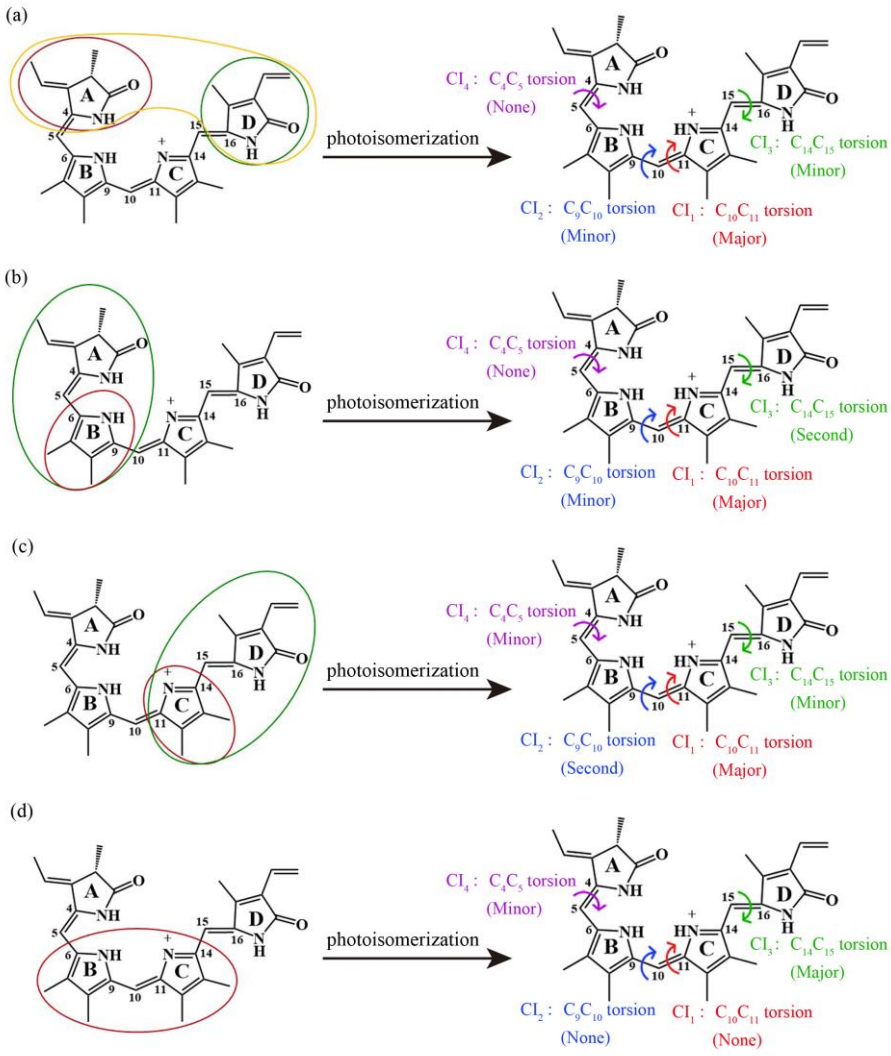

Figure 4. The branching ratios of different CI channels in each group of restricted models. The red, green and yellow circles in the left diagram indicate the constrained moieties. (a) Group 1 includes **Models 0, I**, **IV** and **VIII** (**Model 0** represents the free BV model); (b) Group 2 includes **Models II** and **V**; (c) Group 3 includes **Models III** and **VII**; (d) Group 4 includes **Model VI**.

3.3 Population

The above discussions clearly point out that different decay channels are responsible for the nonadiabatic dynamics of nine constrained BV models. The trajectories follow

distinct reaction channels with different PE profiles, we expect that the evolution of electronic populations of these models should also be different. In principle, the models belonging to the same group should display similar population dynamics, since their underling channels are rather similar.

Figure 5 shows the evolution of a few key dihedral angles with time being, from starting conditions to hopping events. Figure 6 shows their population dynamics. Clearly, the photoisomerization rate is strongly controlled by the dominant CI channel that is significantly modified by different geometric constraints.

Group 1 includes **Models 0, I, IV** and **VIII**. In Group 1, the CI_1 is the most dominant decay channel. As shown in Figure S3, the motion of Ring C is important in the CI_1 channel, while the motion of the Ring B is also involved necessary. The Rings B and C are completely unconstrained in structure, and have no effect on the torsion of the CI_1 channel. Therefore, the nonadiabatic dynamics in this group display the fastest population decay (see Figure 6a). For this group, most trajectories access the CI_1 around 400 fs (Figure 5 a–d). Only for **Model VIII,** we noticed that 9.5% of trajectories stay on the first excited state at the end of simulation. As a consequence, more than 50% of trajectories jump back to the S_0 state within 500 fs, and most of the trajectories return to the ground state within 2000 fs.

Compared with Group 1, the branching ratio towards to the CI_3 channel increased significantly in all models of Group 2, while the CI_1 channel is still the most important one. As depicted in Figure S3, the motion of Ring B plays the visible role in the CI_1 channel, and thus the employment of the constrain in Ring B slows down this channel.

This is confirmed by Figure 5 e and f, which show that the many nonadiabatic transitions at CI_1 take place around 400 fs, while some hops happen at the later time ~400–800 fs. In addition, about 10.0% and 5.2% of the trajectories do not hop back to the ground state for both **Model II** and **V**, respectively. As the result, a slightly longer decay in the population dynamics appears for all models in Group 2. Figure 6b reflects that more than 50% of the trajectories decay to the S_0 state within 700 fs, and most of the trajectories back to the S_0 state at the end of simulation.

In Group 3 (**Models III** and **VII**), the CI_1 channels is still the most dominant one, although its contribution is further decreased in all models. The Ring C is constrained and greatly affects the molecular rotation through the CI_1 channel, see Figure S3. Therefore, the dynamics is quite different with respect to those of the first two groups. The photoisomerization via the CI_1 channel becomes much slower (Figure 5) and many hops take place around 1600 fs (see Figure 5 g and h). And in **Models III** and **VII**, 35.1% and 48.9% of the trajectories do not hop up to 2 ps. Overall, the population decay becomes much slower.

Completely different from the above three groups, CI_1 and CI_2 channels do not exist in the model of Group 4. Here, all trajectories decay visit CI_3 or CI_4. The transitions take place mainly through the CI_3 channel, in which the $C_{15}C_{16}$ double bond rotates more slowly (see Figure 5i). In this case, most hops take place around 1200-1600 fs, and 50% of the trajectories do not jump back to the ground state up to 2 ps. As a consequence, Group 4 shows the slowest decay dynamics in Figure 6d.

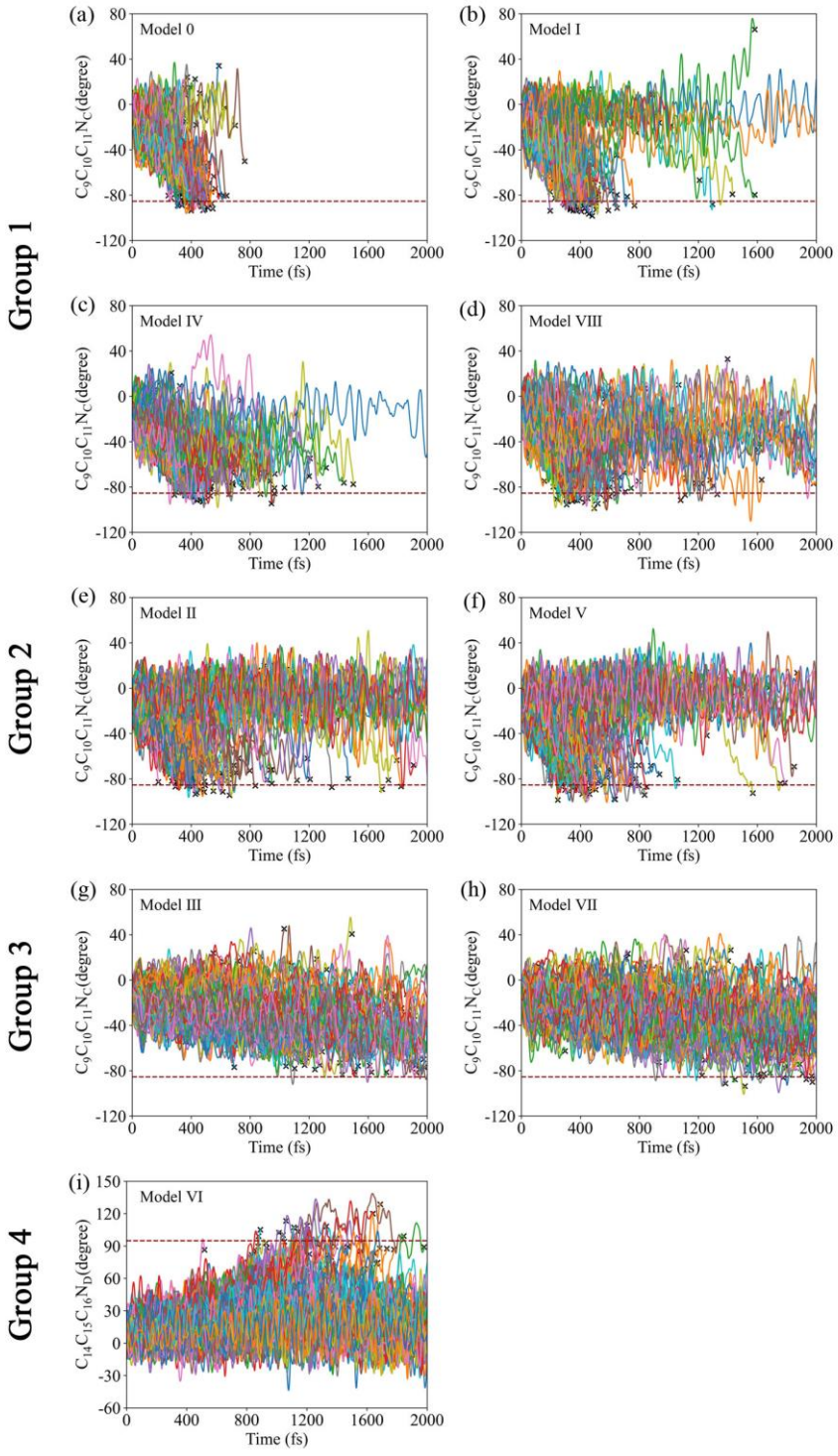

Figure 5. Time evolution of key dihedral angles ($C_9C_{10}C_{11}N_C$ for most models and $C_{14}C_{15}C_{16}N_D$ for Model VI). The red dotted line represents the dihedral angle at the dominant CI structure. The cross labels show the hopping events.

1

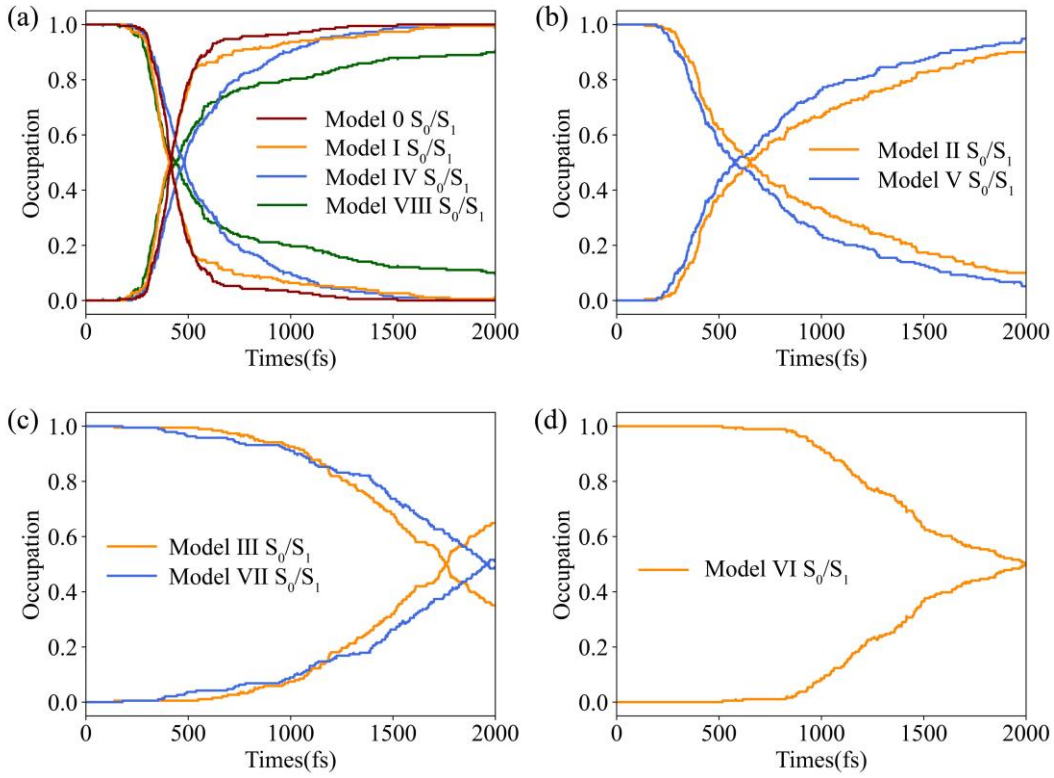

Figure 6. Time-dependent fractional occupations of the S_0 and S_1 electronic states of the nine models in the nonadiabatic dynamics staring from the S_1 state. (a) Group 1; (b) Group 2; (c) Group 3; (d) Group 4.

4. Conclusion

In this work, the photoisomerization processes of BV chromophore are investigated by employing the surface hopping nonadiabatic dynamics simulation at the OM2/MRCI level. Different geometrical constraints are considered, and the corresponding models give distinct decay channels.

The unconstrained BV chromophore (**Model 0)** and the constrained terminal rings (Ring A in **Model I**, Ring D in **IV**, and Rings AD in **VIII**, respectively) have similar

dynamics. The trajectories decay rapidly from S_1 state, with 50% of the trajectories decaying within 500fs. Most trajectories choose to follow the CI_1 channel, characterized by isomerization around $C_{10}C_{11}$ bond.

Models II and **V** constrain the motion of Ring B and the Rings A and B, leading to the slight increasing of the excited-state lifetime with respect to **Models I**, **IV** and **VIII**. Except the major channel via CI_1, the secondary channel is governed by the CI_3 channel, in which the photoisomerization takes place at the $C_{15}C_{16}$ bond.

Models III and **VII**, which are characterized by the restricted motion of Ring C and Rings C and D, show the significantly longer excited-state decay times. Although the CI_1 channel is still the primary channel, the ratio of the CI_2 channel with the photoisomerization at the C_9C_{10} bond increases significantly.

Model VI with the two middle rings fixed show completely different dynamics features, with 50% of the nondecay trajectories at the end of the simulation time 2000 fs. Such slow decay is attributed to the fact that **Model VI** decays mainly through the CI_3 channel in which the $C_{15}C_{16}$ bond torsion is involved.

By simply mechanically restricting the motion of a specific moiety, we try to study the spatial effects of surrounding environment on the photoisomerization dynamics of the BV chromophore with very small computational cost. Our work clearly describes the impact of various possible steric effects on the nonadiabatic dynamics processes. It provides a guideline for the regulation of the photoisomerization reaction channel, which can further propose some novel ideas for the design of phytochrome proteins. In this sense, the current work provides the preliminary but useful understandings of this

important topic efficiently by using a rather simplified method, while it cannot fully and accurately capture the influences of the real biological environment. In order to understand the photoisomerization process of BV chromophore in the protein more realistically, the advanced QM/MM method is the better choice in future research.

Acknowledgments

This work is supported by **NSFC** projects (No. 21903030, 21933011 and 21873112).

Supplementary Material

Key bond lengths and dihedral angles of S_0_min, S_1_min and CI_{1-4}, the structure of S_0_min, S_1_min and CI_{5-6}, excited-state pathways in the CI_5 and CI_6 channels, the time evolution of the normal vector of the rings, the distributions of key dihedral angels at the initial, hopping and CI geometries, cartesian coordinates are available.

References

1 N. C. Rockwell, Y. Su and J. C. Lagarias, *Annu. Rev. Plant Biol.*, 2006, **57**, 837-858.

2 W. L. Butler, K. H. Norris, H. W. Siegelman and S. B. Hendricks, *Proc. Natl. Acad. Sci. U.S.A.*, 1959, **45**, 1703-1708.

3 S. J. Davis, A. V. Vener and R. D. Vierstra, *Science*, 1999, **286**, 2517-2520.

4 Z. Jiang, L. R. Swem, B. G. Rushing, S. Devanathan, G. Tollin and C. E. Bauer, *Science*, 1999, **285**, 406-409.

5 A. Blumenstein, K. Vienken, R. Tasler, J. Purschwitz, D. Veith, N. F. Dinkel and R. Fischer, *Curr. Biol.*, 2005, **15**, 1833-1838.

6 E. A. Rodriguez, G. N. Tran, L. A. Gross, J. L. Crisp, X. Shu, J. Y. Lin and R. Y. Tsien, *Nat. Methods*, 2016, **13**, 763-769.

7 T. Schroeder, *Nature*, 2008, **453**, 345-351.

8 R. Weissleder and M. J. Pittet, *Nature*, 2008, **452**, 580-589.

9 K. G. Chernov, T. A. Redchuk, E. S. Omelina and V. V. Verkhusha, *Chem. Rev.*, 2017, **117**, 6423-6446.

10 A. A. Kaberniuk, A. A. Shemetov and V. V. Verkhusha, *Nat. Methods*, 2016, **13**, 591–597.

11 X. Li, D. Hu, Y. Xie and Z. Lan, *J. Chem. Phys.*, 2018, **149**, 244104.

12 E. V. Gromov and T. Domratcheva, *Phys. Chem. Chem. Phys.*, 2020, **22**, 8535-8544.

13 U. Choudry, D. J. Heyes, S. J. O. Hardman, M. Sakuma, I. V. Sazanovich, J. Woodhouse, E. D. L. Mora, M. N. Pedersen, M. Wulff, M. Weik, G. Schirò and N. S. Scrutton, *Chembiochem*, 2018, **19**, 1036-1043.

14 D. Buhrke, *Phys. Chem. Chem. Phys.*, 2021, **23**, 20867-20874.

15 D. Buhrke, N. N. Tavraz, D. M. Shcherbakova, L. Sauthof, M. Moldenhauer, F. V. Escobar, V. V. Verkhusha, P. Hildebrandt and T. Friedrich, *Sci. Rep.*, 2019, **9**, 1866.

16 R. González and M. A. Mroginski, *J. Phys. Chem. B*, 2019, **123**, 9819-9830.

17 D. Wang, X. Li, L. Wang, X. Yang and D. Zhong, *J. Phys. Chem. Lett.*, 2020, **11**, 8819-8824.

18 D. Wang, Y. Qin, M. Zhang, X. Li, L. Wang, X. Yang and D. Zhong, *J. Phys. Chem.*

Lett., 2020, **11**, 5913−5919.

19 J. A. Ihalainen, E. Gustavsson, L. Schroeder, S. Donnini, H. Lehtivuori, L. Isaksson, C. Thöing, V. Modi, O. Berntsson, B. S. Buchli, A. Liukkonen, H. Häkkänen, E. Kalenius, S. Westenhoff and T. Kottke, *J. Am. Chem. Soc.*, 2018, **140**, 12396-12404.

20 C. Kneip, P. Hildebrandt, W. Schlamann, S. E. Braslavsky, F. Mark and K. Schaffner, *Biochemistry*, 1999, **38**, 15185-15192.

21 J. R. Wagner, J. S. Brunzelle, K. T. Forest and R. D. Vierstra, *Nature*, 2005, **438**, 325-331.

22 G. Cornilescu, A. T. Ulijasz, C. C. Cornilescu, J. L. Markley and R. D. Vierstra, *J. Mol. Biol.*, 2008, **383**, 403-413.

23 A. T. Ulijasz, G. Cornilescu, C. C. Cornilescu, J. Zhang, M. Rivera, J. L. Markley and R. D. Vierstra, *Nature*, 2010, **463**, 250-254.

24 X. Yang, Z. Ren, J. Kuk and K. Moffat, *Nature*, 2011, **479**, 428-432.

25 E. S. Burgie, A. N. Bussell, J. M. Walker, K. Dubiel, and R. D. Vierstra, *Proc. Natl. Acad. Sci. U.S.A.*, 2014, **111**, 10179-10184.

26 H. Takala, A. Björling, O. Berntsson, H. Lehtivuori, S. Niebling, M. Hoernke, I. Kosheleva, R. Henning, A. Menzel, J. A. Ihalainen and S. Westenhoff, *Nature*, 2014, **509**, 245-248.

27 G. Salvadori, V. Macaluso, G. Pellicci, L. Cupellini, G. Granucci and B. Mennucci, *ChemRxiv*, 2022.

28 D. Morozov, V. Modi, V. Mironov and G. Groenhof, *J. Phys. Chem. Lett.*, 2022, **13**, 4538-4542.

29 V. Macaluso, G. Salvadori, L. Cupellini and B. Mennucci, *Chem. Sci.*, 2021, **12**, 5555-5565.

30 B. Durbeej, *Phys. Chem. Chem. Phys.*, 2009, **11**, 1354-1361.

31 A. Strambi and B. Durbeej, *Photochem. Photobiol. Sci.*, 2011, **10**, 569-579.

32 X. Zhuang, J. Wang and Z. Lan, *J. Phys. Chem. B*, 2013, **117**, 15976-15986.

33 H. Huang, C. Xu, K. Lin, J. Peng, F. L. Gu and Z. Lan, *ChemRxiv*, 2022.

34 X. Liu, T. Zhang, Q. Fang, W. Fang, L. González and G. Cui, *Angew. Chem. Int. Ed.*, 2021, **60**, 18688-18693.

35 X. Yang, E. A. Stojkovic, J. Kuk and K. Moffat, *Proc. Natl. Acad. Sci. U.S.A.*, 2007, **104**, 12571-1257.

36 K. Fushimi, T. Miyazaki, Y. Kuwasaki, T. Nakajima, T. Yamamoto, K. Suzuki, Y. Ueda, K. Miyake, Y. Takeda, J. H. Choi, H. Kawagishi, E. Y. Park, M. Ikeuchi, M. Sato and R. Narikawa, *Proc. Natl. Acad. Sci. U.S.A.*, 2019, **116**, 8301-8309.

37 X. Shu, A. Royant, M. Z. Lin, T. A. Aguilera, V. L. Ram, P. A. Steinbach and R. Y. Tsien, *Science*, 2009, **324**, 804-807.

38 F. F. JÖbsis, *Science*, 1977, **198**, 1264-1267.

39 R. Weissleder and V. Ntziachristos, *Nat. Med.*, 2003, **9**, 123-128.

40 H. M. Senn and W. Thie, *Angew. Chem. Int. Ed.*, 2009, **48**, 1198-1229.

41 R. C. Otero and M. Barbatti, *Chem. Rev.*, 2018, **118**, 7026-7068.

42 E. Brunk and U. Rothlisberger, *Chem. Rev.*, 2015, **115**, 6217-6263.

43 J. Gao, *Acc. Chem. Res.*, 1996, **29**, 298-305.

44 J. Gao and D. G. Truhlar, *Annu. Rev. Phys. Chem.*, 2002, **53**, 467-505.

45 A. Warshel, *Nature*, 1976, **260**, 679-683.

46 J. J. Szymczak, M. Barbatti and H. Lischka, *J. Chem. Theory Comput.*, 2008, **4**, 1189-1199.

47 M. Barbatti, M. Ruckenbauer, J. J. Szymczak, A. J. A. Aquino and H. Lischka, *Phys. Chem. Chem. Phys.*, 2008, **10**, 482-494.

48 M. Barbatti and H. Lischka, *J. Phys. Chem. A*, 2007, **111**, 2852-2858.

49 M. Barbatti and H. Lischka, *J. Am. Chem. Soc.*, 2008, **130**, 6831-6839.

50 W. Weber and W. Thiel, *Theor. Chem. Acc.*, 2000, **103**, 495–506.

51 A. Koslowski, M. E. Beck and W. Thiel, *J. Comput. Chem.*, 2003, **24**, 714-726.

52 G. Granucci and M. Persico, *J. Chem. Phys.*, 2007, **126**, 134114.

53 T. W. Keal, A. Koslowski and W. Thiel, *Theor. Chem. Acc.*, 2007, **118**, 837-844.

54 W. Thiel, MNDO99 program, 2020, Max-Planck-Institut für Kohlenforschung, Mülheim an der Ruhr, *Germany*, 2020.

55 S. Xia, B. Xie, Q. Fang, G. Cui and W. Thiel, *Phys. Chem. Chem. Phys.*, 2015, **17**, 9687-9697.

56 E. P. Wigner, in Part I: *Phys. Chem*. Part II: *Solid State Physics*, Springer, 1997, 110-120.

57 J. C. Tully, *J. Chem. Phys.*, 1990, **93**, 1061-1071.

58 G. Granucci and M. Persico, *J. Chem. Phys.*, 2007, **126**, 134114.

59 L. Du and Z. Lan, *J. Chem. Theory Comput.*, 2015, **11**, 1360-1374.